INTERNATIONAL JOURNAL FOR NUMERICAL METHODS IN FLUIDS
Int. J. Numer. Meth. Fluids 2010; **63**:468–494
Published online 1 June 2009 in Wiley InterScience (www.interscience.wiley.com). DOI: 10.1002/fld.2085

A high-fidelity low-cost aerodynamic model using proper orthogonal decomposition

M. J. Mifsud*,†, S. T. Shaw and D. G. MacManus

School of Engineering, Cranfield University, Bedford, MK43 0AL, U.K.

SUMMARY

In this paper a high-fidelity aerodynamic model is presented for use in parametric studies of weapon aerodynamics. The method employs a reduced-order model obtained from the proper orthogonal decomposition (POD) of an ensemble of computational fluid dynamics (CFD) solutions with varying parameters. This decomposition produces an optimal linear set of orthogonal basis functions that best describe the ensemble of numerical solutions. These solutions are then projected onto this set of basis functions to provide a finite set of scalar coefficients that represent the solutions. A pseudo-continuous representation of these projection coefficients is constructed, which allows predictions to be made of parameter combinations not in the original set of observations. The paper explores the performance of a few design-of-experiment approaches for the generation of the initial ensemble of computational experiments. Response surface construction methods based on parametric and non-parametric models for the pseudo-continuous representation of the projection coefficients are also evaluated. The model has been applied to two-flow problems related to high-speed weapon aerodynamics, inviscid flow around a flare-stabilized hypersonic projectile and supersonic turbulent flow around a fin-stabilized projectile with drooping nose control. Comparisons of model predictions with high-fidelity CFD simulations suggest that the POD provides a reliable and robust approach to the construction of reduced-order models. The practicality of the model is shown to be sensitive to the technique used to generate the ensemble of observations from which the model is constructed, while the accuracy of the approach depends on the pseudo-continuous representation of the projection coefficients. Copyright © 2009 John Wiley & Sons, Ltd.

Received 25 March 2008; Revised 22 January 2009; Accepted 4 April 2009

KEY WORDS: reduced-order modelling; proper orthogonal decomposition; singular value decomposition; response surfaces; linear regression; radial basis functions

*Correspondence to: M. J. Mifsud, School of Engineering, Cranfield University, Bedford, MK43 0AL, U.K.
†E-mail: michaelmifsud19@hotmail.com

Contract/grant sponsor: Defence Science and Technology Laboratory (DSTL)
Contract/grant sponsor: QinetiQ Ltd

1. INTRODUCTION

The design of modern air-vehicles is a complex process that requires the successful integration of numerous disparate disciplines, for example propulsion, aerodynamics, structural mechanics and flight mechanics. The inter-disciplinary nature of the problem is such that assessing the performance of an individual configuration using high-fidelity analysis tools is expensive and frequently severely limits the extent to which the design space can be explored during the development cycle. To overcome these limitations, it is a common practice to either degrade the analysis model (for example solving Euler equations instead of Navier–Stokes equations to obtain the aerodynamics) or restrict the design space. The former has clear implications for modelling fidelity, while the latter, which relies on engineering judgment, may lead to sub-optimal designs.

An alternative approach is the use of meta-modelling strategies that attempt to construct a pseudo-closed-form model from the output of the high-fidelity analysis tool at discrete points in the design space. The meta-model is then used as a low-cost surrogate for the original analysis tool within the multi-disciplinary framework. In the context of aerodynamic simulations a number of meta-modelling approaches have been proposed, see for example the review of Vavalle [1]. However, the majority of such approaches simply provide models for individual design target functions, such as integrated forces and moments, rather than for the full flowfield output of the analysis tool.

In this work a meta-model of a computational fluid dynamics (CFD) tool, Cranfield University's IMPNS space-marching solver, is presented. The method employs a reduced-order model based upon the properties of proper orthogonal decomposition (POD) [2] to characterize an ensemble of computational experiments. The reduced-order model is adapted for predictions through the construction of a response surface of the projection coefficients that span the parametric space of interest.

The model is applied to two problems related to high-speed weapon aerodynamics. The first concerns inviscid flow over the axi-symmetric flare stabilized projectile studied by Schmidt *et al.* [3] and Plostins *et al.* [4]. This test case was selected as it is the one for which existing semi-empirical modelling tools perform poorly and therefore poses a reasonable challenge to the currently proposed approach. The configuration is studied for a parameter space that involves changes to both the free-stream conditions (Mach number and incidence) and geometry (base radius). The results of the study are used to demonstrate the effectiveness of POD as a reduced-order model for weapon aerodynamics at supersonic and hypersonic Mach numbers. For this problem the relative performances of elements of the model, for example the sampling technique and the choice of pseudo-continuous surface representation, are also explored.

The second problem relates to a more complex configuration investigated experimentally by Landers *et al.* [5] and computationally by Shoesmith *et al.* [6]. This configuration consists of a 4 calibre 0.7 power series nose with a 19.5 calibre cylindrical section with 8 stabilizing fins. The nose is free to rotate providing a means of control. The fluid dynamics of this configuration is complex involving oblique shocks, boundary layers and vortices and their interactions. For this case two parameters, the nose deflection in the pitch plane and the flow angle of attack, were varied, and the ability of the model to predict not only the forces and moments but also flow-field information was explored.

The results presented in this paper demonstrate how a small number of CFD solutions can be used together with POD to generate aerodynamic data with low cost and high accuracy.

DOI: 10.1002/fld

2. NUMERICAL METHODS

2.1. CFD model

The objective of this work was to obtain a high-fidelity low-cost surrogate of a CFD analysis tool, namely the IMPNS flow solver [7, 8]. The IMPNS software has been developed to provide a practical flow solver (rapid, robust and accurate) for problems in high-speed external weapon aerodynamics.

IMPNS provides algorithms for the solution of the Euler, Thin-layer or Parabolized Navier Stokes equations together with a range of turbulence closures that includes the algebraic model of Baldwin and Lomax [9] enhanced with modifications due to either Degani and Schiff [10] or Qin and Jayatunga [11], variants of the one-equation model of Spalart and Allmaras [12] and Wilcox's two-equation k-ω model [13]. The turbulence closure is coupled with the mean flow equations in a segregated fashion.

The governing equations are formulated for a finite control volume and solved using an implicit space marching procedure. For flows in which there is no upstream influence, a single sweep is employed starting at the nose of the configuration and proceeding in the stream-wise direction. The approach has been extended to allow for flows with upstream influence, for example blunt body flows and flows exhibiting axial separation. In this case a multi-sweep procedure in which the solver marches backwards and forwards is employed to capture the elliptic characteristics of the governing equations. A combination of single sweep and multi-sweep strategies can be used to solve for flows that contain embedded regions of flow where upstream influence is important.

IMPNS provides a number of schemes that can be employed in the spatial discretization, see for example Qin and Ludlow [14]. In the present calculations, the spatial discretization is performed using an approximate Riemann solver based on the work of Osher and Solomon [15] together with a central difference-based scheme for the viscous fluxes. An implicit system of equations arises at each marching plane following the spatial discretization. This system is solved using a relaxation approach in which an additional pseudo-time derivative is added to the steady governing equations. The implicit system is then solved by marching to the steady state in pseudo-time. Convergence of the pseudo-time relaxation is accelerated through the use of a combination of an implicit Newton–Krylov method [16] and full multi-grid [17].

IMPNS uses standard structured multi-block grids. To provide geometric flexibility and to reduce computational expense, non-matching block faces are permitted in the stream-wise direction. This permits changes of grid topology in the stream-wise direction, allowing the grid to conform to the geometric characteristics of the configuration being studied. IMPNS has been used extensively to study the aerodynamics of high-speed weapon configurations with remarkable success; further details of its development and application can be found in references [18–24].

2.2. Meta-model

The meta-model consists of three main elements: a technique for sampling the parameter space using a design-of-experiment approach, a reduced-order model that can be used to represent the dominant dynamical characteristics of the system described by a set of discrete observations at the sample points and a pseudo-continuous representation of the scalar coefficients obtainable from the reduced-order model.

2.2.1. The reduced-order model: *POD.* In fluid mechanics the POD was first introduced by Lumley [25] in the context of stochastic turbulence. The same procedure has been widely used in other

DOI: 10.1002/fld

disciplines and is commonly referred to as the Karhunen–Loéve expansion and the principal component analysis. POD is also very closely related to the singular value decomposition (SVD). The method provides a foundation for the modal decomposition of a system of functions, usually data obtained from either experiments or numerical simulations. The resulting basis functions are called proper orthogonal modes and are the best possible uncorrelated and data-dependent linear set of basis functions that describe the initial observations.

The POD method has been used extensively in the fields of random variables, image processing, data compression and system controls. In the field of fluid dynamics, it has been used in unsteady flow problems such as aero-elasticity and stochastic turbulence to capture the variation in time of fluid flow. Less frequent is the use and development of reduced-order models to capture parametric variations. Epureanu *et al.* [26] employed POD to develop reduced-order models for potential flow in turbo-machinery with sampling over a range of inter-blade phase angles and time. The resulting models were applied to flows at varying Mach numbers, even though the observational ensemble was computed at a single Mach number and accurate results were obtained at Mach numbers close to that used in the initial observations. LeGresley and Alonso [27] used POD to develop surrogate models of a 2D Euler solver for design optimization purposes. In this case the POD modes spanned a range of aerofoil geometries. More recently, Bui-Thanh *et al.* [28] employed the POD method together with an interpolation procedure to predict the pressure flow-field over an aerofoil for varying inflow Mach number and angle of attack.

The POD procedure is most of the time described using the calculus of variations applied to a multi-dimensional spatio-temporal data set. In such problems, the data set is produced from solution vectors obtained at a particular instant of time. In this paper, the POD is described for steady-state problems in terms of the SVD. Although these two approaches are equivalent, the SVD approach is preferred as it is more straightforward.

Considering an ensemble of data $\mathbf{A}(\mathbf{Y}(\mathbf{x}))$ where $\mathbf{A}\in\mathbf{R}^{m,xn}$ is obtained from the solutions $\mathbf{Y}(\mathbf{x})$ of a high-fidelity model at various design points $\mathbf{x}^{(1)},\mathbf{x}^{(2)},\ldots,\mathbf{x}^{(m)}$ where $\mathbf{Y}\in\mathbf{R}^{n}$ represents the solution vector of primitive or conservative field variables and $\mathbf{x}\in\mathbf{R}^{r}$ represents the vector of different design variables or parameters, the ensemble of data is formed as follows:

$$\mathbf{A}(\mathbf{Y}(\mathbf{x}))=\begin{pmatrix}\mathbf{Y}(\mathbf{x}^{(1)})\\ \mathbf{Y}(\mathbf{x}^{(2)})\\ \vdots\\ \mathbf{Y}(\mathbf{x}^{(m)})\end{pmatrix} \tag{1}$$

where $\mathbf{Y}(\mathbf{x}^{(i)})=\{\mathbf{Y}_1(\mathbf{x}^{(i)}),\mathbf{Y}_2(\mathbf{x}^{(i)}),\ldots,\mathbf{Y}_n(\mathbf{x}^{(i)})\}$, n is the number of grid points over which the computational calculation is performed and m is the number of realizations or parameters' combination.

The sub-space spanned by these solutions can be used to approximate $\mathbf{Y}$ by representing it in terms of orthogonal basis functions or vectors $\mathbf{\Phi}$ that span the parameter space of interest.

$$\mathbf{\Phi}=\mathbf{span}\{\mathbf{Y}(\mathbf{x}^{(1)}),\mathbf{Y}(\mathbf{x}^{(2)}),\mathbf{Y}(\mathbf{x}^{(3)}),\ldots,\mathbf{Y}(\mathbf{x}^{(m)})\} \tag{2}$$

In POD each realization or solution vector is referred to as a snapshot.

DOI: 10.1002/fld

The objective of the POD is to obtain a set of m optimal basis vectors that span the subspace formed by m snapshots. In this context the snapshots are obtained for different values of the parameters, so that the solution at a particular parameter can be reconstructed as

$$\mathbf{Y} = \langle \mathbf{Y} \rangle + \sum_{i=1}^{m} \boldsymbol{\alpha}_i \boldsymbol{\Phi}_i \tag{3}$$

where $\langle \mathbf{Y} \rangle = 1/m \sum_{i=1}^{m} \mathbf{Y}(\mathbf{x}^{(i)})$ is the arithmetic mean of the vector of field variables at each grid point across the whole set of snapshots, $\boldsymbol{\Phi}_i, i = 1, 2, \ldots, m$ denotes the set of basis vectors at a particular grid point and $\boldsymbol{\alpha}_i, i = 1, 2, \ldots, m$ are scalar coefficients to be determined. Hence a snapshot can be reconstructed by adding up the contribution from each basis vector in turn at each grid point.

Defining a set of modified snapshots obtained by subtracting $\langle \mathbf{Y} \rangle$ from $\mathbf{Y}(\mathbf{x}^{(i)})$,

$$\tilde{\mathbf{Y}}^{(i)} = \mathbf{Y}(\mathbf{x}^{(i)}) - \langle \mathbf{Y} \rangle, \quad i = 1, 2, \ldots, m \tag{4}$$

where m is total number of snapshots.

Let $\mathbf{A} \in \mathbf{R}^{mxn}$ denote the matrix whose rows are the modified snapshots. Each snapshot is constructed by placing in order the solution at each grid point for the whole grid. This order can be determined arbitrarily, but is subject to the constraint that it must be consistent throughout the whole set of snapshots.

$$\mathbf{A} = \begin{pmatrix} \tilde{Y}_1^{(1)} & \ldots & \tilde{Y}_n^{(1)} \\ \tilde{Y}_1^{(2)} & \ldots & \tilde{Y}_n^{(2)} \\ \tilde{Y}_1^{(3)} & \ldots & \tilde{Y}_n^{(3)} \\ \cdot & \ldots & \cdot \\ \tilde{Y}_1^{(m)} & \ldots & \tilde{Y}_n^{(m)} \end{pmatrix} \tag{5}$$

The SVD of $\mathbf{A}$ can be written as

$$\mathbf{A} = \mathbf{U}\boldsymbol{\Sigma}\mathbf{V}^{\mathrm{T}} \tag{6}$$

where $\mathbf{U} \in \mathbf{R}^{mxm}$ and $\mathbf{V} \in \mathbf{R}^{nxn}$ are orthogonal matrices. These matrices are the left and right singular vectors, respectively. $\boldsymbol{\Sigma} \in \mathbf{R}^{mxn}$ is a diagonal matrix whose diagonal elements consist of $q = \min(m, n)$ non-negative numbers σ_i arranged in decreasing order; that is,

$$\sigma_1 \geqslant \sigma_2 \geqslant \sigma_3 \geqslant \cdots \geqslant \sigma_q$$

DOI: 10.1002/fld

σ_i are referred to as the singular values of $\mathbf{A}$, hence the name SVD. In expanded matrix form the SVD of $\mathbf{A}$ can be expressed as follows:

$$\begin{pmatrix} \tilde{Y}_1^{(1)} & \dots & \tilde{Y}_n^{(1)} \\ \tilde{Y}_1^{(2)} & \dots & \tilde{Y}_n^{(2)} \\ \tilde{Y}_1^{(3)} & \dots & \tilde{Y}_n^{(3)} \\ \cdot & \dots & \cdot \\ \tilde{Y}_1^{(m)} & \dots & \tilde{Y}_n^{(m)} \end{pmatrix} = \begin{pmatrix} u_{11} & \dots & u_{1m} \\ u_{21} & \dots & u_{2m} \\ u_{31} & \dots & u_{3m} \\ \cdot & \dots & \cdot \\ u_{m1} & \dots & u_{mm} \end{pmatrix} \begin{pmatrix} \sigma_1 & 0 & 0 & 0 & 0 & 0 & \cdot & 0 \\ 0 & \sigma_2 & 0 & 0 & 0 & 0 & \cdot & 0 \\ 0 & 0 & \sigma_3 & 0 & 0 & 0 & \cdot & 0 \\ \cdot & \cdot & \cdot & \cdot & \cdot & \cdot & \cdot & \cdot \\ 0 & 0 & 0 & 0 & \sigma_m & 0 & \cdot & 0 \end{pmatrix}$$

$$\times \begin{pmatrix} v_{11} & \dots & v_{1n} \\ v_{21} & \dots & v_{2n} \\ v_{31} & \dots & v_{3n} \\ \cdot & \dots & \cdot \\ \cdot & \dots & \cdot \\ \cdot & \dots & \cdot \\ v_{n1} & \dots & v_{nn} \end{pmatrix}$$

This is the full form of the SVD. Since $\mathbf{\Sigma}$ is a diagonal $m \times n$ matrix, then the above matrix equation can be written in reduced form as follows if we assume that $m < n$:

$$\begin{pmatrix} \tilde{Y}_1^{(1)} & \dots & \tilde{Y}_n^{(1)} \\ \tilde{Y}_1^{(2)} & \dots & \tilde{Y}_n^{(2)} \\ \tilde{Y}_1^{(3)} & \dots & \tilde{Y}_n^{(3)} \\ \cdot & \dots & \cdot \\ \tilde{Y}_1^{(m)} & \dots & \tilde{Y}_n^{(m)} \end{pmatrix} = \begin{pmatrix} u_{11} & \dots & u_{1m} \\ u_{21} & \dots & u_{2m} \\ u_{31} & \dots & u_{3m} \\ \cdot & \dots & \cdot \\ u_{m1} & \dots & u_{mm} \end{pmatrix} \begin{pmatrix} \sigma_1 & 0 & 0 & \cdot & 0 \\ 0 & \sigma_2 & 0 & \cdot & 0 \\ 0 & 0 & \sigma_3 & \cdot & 0 \\ \cdot & \cdot & \cdot & \cdot & \cdot \\ 0 & 0 & 0 & \cdot & \sigma_m \end{pmatrix}$$

$$\times \begin{pmatrix} v_{11} & \dots & v_{1n} \\ v_{21} & \dots & v_{2n} \\ v_{31} & \dots & v_{3n} \\ \cdot & \dots & \cdot \\ v_{m1} & \dots & v_{mn} \end{pmatrix}$$

where the matrices $\mathbf{\Sigma}$ and $\mathbf{V}^{\mathrm{T}}$ are reduced in size. The columns of $\mathbf{V}$ and hence the rows of $\mathbf{V}^{\mathrm{T}}$ are the proper orthogonal modes of the system. Hence the set of basis vectors $\mathbf{\Phi}_i = \mathbf{V}^{\mathrm{T}}(i,:) \in \mathbf{R}^n$. These basis vectors are of unit magnitude and orthogonal, hence orthonormal.

DOI: 10.1002/fld

Writing the product of $\mathbf{U}$ and $\mathbf{\Sigma}$ as a matrix $[\alpha_{ij}]$

$$\begin{pmatrix} \tilde{Y}_1^{(1)} & \dots & \tilde{Y}_n^{(1)} \\ \tilde{Y}_1^{(2)} & \dots & \tilde{Y}_n^{(2)} \\ \tilde{Y}_1^{(3)} & \dots & \tilde{Y}_n^{(3)} \\ \cdot & \dots & \cdot \\ \tilde{Y}_1^{(m)} & \dots & \tilde{Y}_n^{(m)} \end{pmatrix} = \begin{pmatrix} \alpha_{11} & \dots & \alpha_{1m} \\ \alpha_{21} & \dots & \alpha_{2m} \\ \alpha_{31} & \dots & \alpha_{3m} \\ \cdot & \dots & \cdot \\ \alpha_{m1} & \dots & \alpha_{mm} \end{pmatrix} \begin{pmatrix} v_{11} & \dots & v_{1n} \\ v_{21} & \dots & v_{2n} \\ v_{31} & \dots & v_{3n} \\ \cdot & \dots & \cdot \\ v_{m1} & \dots & v_{mn} \end{pmatrix} \tag{7}$$

which has the form of $\tilde{Y}_k^{(i)} = \sum_{j=1}^{m} \alpha_{ij} v_{jk}$. Thus, the scalar coefficients are obtained directly from the multiplication of $\mathbf{U}$ and $\mathbf{\Sigma}$. From the SVD of $\mathbf{A}$ it can be noticed that since $\mathbf{V}$ is an orthogonal matrix, the transpose of $\mathbf{V}$ is equal to its inverse i.e. $\mathbf{V^T} = \mathbf{V}^{-1}$, therefore

$$\mathbf{AV} = \mathbf{U\Sigma} \tag{8}$$

that is,

$$\alpha_{ij} = \tilde{\mathbf{Y}}^{(i)} \cdot \mathbf{\Phi}_j \tag{9}$$

where $\mathbf{\Phi}_j = \mathbf{V}(:, j) \in R^n$. The scalar coefficients α_{ij} are also referred to as projection coefficients because these are obtained by projecting the solution onto the basis vectors. A complete reconstruction of the snapshots can be obtained from

$$\mathbf{Y} = \langle \mathbf{Y} \rangle + \tilde{\mathbf{Y}} \tag{10}$$

Now, $\mathbf{Y}$ may represent a vector of scalar functions such as the primitive or conservative variables and therefore the method described can be applied to each variable in turn to form a distinct basis for each variable. However, an improvement in the ability of the basis to represent the system may be achieved by considering not only how the individual variables vary from one snapshot to another but also how variables change relative to one another. Hence $\mathbf{Y}$ is developed from state variable vectors consisting of all the primitive or conservative variables [27]. In this case, the POD modes are sensitive to the scaling of the flow variables as these are in different units and have significantly varying magnitudes. Consequently, appropriate scaling factors are necessary for each fluctuating flow variable that makes their magnitude of the same order [29].

If a problem is represented by a suitable number of snapshots from which a suitably rich set of basis vectors is available, the singular values become small rapidly and a small number of basis vectors are adequate to reconstruct and approximate the snapshots. In this way, POD provides an efficient means of capturing the dominant features of a multi-degree of freedom system and representing it to the desired precision by using the relevant set of modes, thus reducing the order of the system. In other words, the reduced-order model is derived by projecting the CFD model onto a reduced space spanned by only some of the proper orthogonal modes or POD eigenfunctions.

Assuming that p modes that correspond to the largest p singular values are dominant, then the energy E or variance in the data captured by the first p modes can be computed as

$$E(p) = \frac{\sum_{i=1}^{i=p} \sigma_i^2}{\sum_{i=1}^{i=m} \sigma_i^2} \tag{11}$$

DOI: 10.1002/fld

If this energy is high say over 99% of the total energy, then p modes are adequate to capture the principal features and approximately reconstruct the data set. Thus, a reduced subspace is formed that is only spanned by p modes.

Instead of the SVD approach, the proper orthogonal modes can also be computed by solving for the largest p eigenvalues and corresponding eigenvectors of the matrix $\mathbf{K}=\mathbf{A}^{\mathrm{T}}\mathbf{A}\in\mathbf{R}^{nxn}$ where $\mathbf{A}^{\mathrm{T}}\mathbf{A}=\mathbf{V}\boldsymbol{\Sigma}^2\mathbf{V}^{\mathrm{T}}$. Hence it follows that $\mathbf{V}$ is the matrix of eigenvectors of $\mathbf{K}$ and $\sigma_i^2,\ i=1,2,\ldots,m$, are its eigenvalues. For cases where $m\ll n$, instead of using the SVD procedure, it is computationally more efficient to use the 'method of snapshots' proposed by Sirovich [30]. In this approach an $m\times m$ eigenvalue problem $\mathbf{A}\mathbf{A}^{\mathrm{T}}\mathbf{U}=\boldsymbol{\Sigma}^2\mathbf{U}$ is formed, from which $\mathbf{U}$ is computed. Hence, pre-multiplying by $\mathbf{U}^{\mathrm{T}}$ Equation (6) we get $\mathbf{U}^{\mathrm{T}}\mathbf{A}=\boldsymbol{\Sigma}\mathbf{V}^{\mathrm{T}}$. Therefore, the first m rows of $\mathbf{U}^{\mathrm{T}}\mathbf{A}$ normalized to unit magnitude represent the proper orthogonal modes.

When the domain between snapshots is different, that is there exists a geometrical change between snapshots, the modes derived from the snapshots will no longer remain at fixed places within the computational domain and consequently an error is introduced in this modelling technique being a space-index transformation. One approach to this problem is to use a common domain for every snapshot and apply transpiration boundary conditions to account for the changes in the boundary. However, in this work the method as suggested and adopted by LeGresley and Alonso [27] has been adopted.

Using this model reduction technique, a low-dimensional system is produced that has the same essential characteristics as the original system but with far less storage requirements and a much lower evaluation time.

2.2.2. Pseudo-continuous representation. The use of reduced-order models based upon the POD for prediction requires the transformation of the projection coefficients, α_i, from the discrete sample space for which they have been computed to a continuous space. If α_i varies as a smooth function with the change in parameters, then a meta-model may be used to determine the POD projection coefficients at intermediate parametric values not included in the original data ensemble. The predicted solution vector $\mathbf{Y}(\mathbf{x}^{(\beta)})$ for any variable β within the parametric space is given by

$$\mathbf{Y}(\mathbf{x}^{(\beta)})=\langle\mathbf{Y}\rangle+\sum_{i=1}^{p'}\alpha_i^{\beta}\boldsymbol{\Phi}_i \tag{12}$$

where p' is normally greater than p and the weighting coefficients α_i^{β} are found using the meta-model.

A variety of meta-modelling techniques suitable for this purpose are described in the literature of which the response surface methodology (RSM) has found general acceptance. The RSM is a statistical tool originally developed for experimental design and subsequently adapted to approximate computational simulations. The RSM is founded on the assumption that the data can be described by a set of simple basis functions, such as second-order polynomials, that are fitted to the data ensemble using a least-squares regression technique.

While regression techniques work well for experimental data, where noise due to random errors is smoothed out from the data, they are less appropriate when dealing with the results from deterministic numerical simulations or when working with complex data sets. Of particular concern in the context of the present work are two problems: first that the response surface constructed using regression analysis may not exactly fit the sample data from which it has been constructed and second that the method smoothes local variations in the data.

DOI: 10.1002/fld

To investigate and understand these problems, further three parametric/non-parametric meta-models were also explored, spline interpolation methods and radial basis functions (RBFs). In the latter case multi-quadric, polyharmonic and gaussian kernels were considered. All these models produce an interpolative fit through all of the sample points and provide improved representations of data sets that have localized minima and maxima.

2.2.2.1. Response surface construction methods

A. Linear regression models: Given a set of data points $\mathbf{x}^{(i)} \in \mathbf{R}^r$ where $i = 1, \ldots, m$ and the corresponding function values $f(\mathbf{x}^{(i)})$, a global approximation function $\tilde{f}(\mathbf{x}^{(i)})$ can be obtained by considering a second-order polynomial as a model such as

$$\tilde{f}(\mathbf{x}^{(i)}) = c_0 + \sum_{i=1}^{r} c_i x_i + \sum_{i=1}^{r} c_{ii} x_i^2 + \sum_{i=1}^{r} \sum_{\substack{j=1 \\ j \neq i}}^{r} c_{ij} x_i x_j \tag{13}$$

where the c's are unknown coefficients determined by the least-squares approach. In this case the function values $f(\mathbf{x}^{(i)})$ are the scalar coefficients α_i obtained by projecting the expensive solution onto the proper orthogonal modes. The response surface equation can then be used to determine the projection coefficients at any arbitrary parameter values. This technique is generally inadequate in providing a globally accurate representation because of its smoothing effect; hence, interpolating models were also considered.

B. Interpolating models: Generally, an interpolating model satisfies the following condition:

$$\tilde{f}(x^{(i)}) = f(x^{(i)}), \quad i = 1, \ldots, m \tag{14}$$

which shows that the function and the approximation are equal at all data points. Two different interpolating methods were considered.

(i) Spline interpolation: In spline interpolation, the interpolant is a special type of piecewise polynomial referred to as a spline. Spline interpolation requires that the data points will be on a grid-like pattern.

(a) Linear spline interpolation: This is equivalent to a piecewise linear interpolation where the data points are connected with straight lines.

(b) Cubic spline interpolation: In cubic spline interpolation, a cubic polynomial is used in each interval between two consecutive data points. One cubic polynomial has four coefficients to be determined, hence requires four conditions. Two of these are obtained from the data points at each end of the interval. The other two are obtained from the requirement that the first and second derivatives of the polynomial become continuous across each data point, hence obtaining a smooth curve.

(ii) Radial basis functions: An RBF [31] is a real-valued function whose value depends on the Euclidean distance from some point called a centre. RBFs are typically used to build up function approximation of the form

$$\tilde{f}(x) = p(x) + \sum_{i=1}^{N} w_i \Psi(\|x - x_i\|) \tag{15}$$

where the approximating function $\tilde{f}(x)$ is represented as a sum of N RBFs Ψ, each associated with a different centre x_i and weighted by an appropriate coefficient $w_i . p(x)$

DOI: 10.1002/fld

is a polynomial of one degree less than the RBF and is included to ensure a unique solution for the weight vector. Thus, an RBF is a weighted sum of translations of a radially symmetric basis function augmented by a polynomial term. In particular RBFs are suitable for interpolating scattered data and hence do not require the data to lie on any sort of regular grid for most types.

Typical RBFs are

(i) Gaussian $\Psi(r)=\mathrm{e}^{-r/\theta^2}$

(ii) multi-quadric [31, 32] $\Psi(r)=\sqrt{1+r/\theta^2}$ and

(iii) polyharmonics such as the triharmonic $\Psi(r)=r^3$

The constant θ in (i) and (ii) is called the shape parameter. The RBF interpolant $\tilde{f}(x)$ is defined by the coefficients of the polynomial $p(x)$ and the weights w_i. Since this produces an under-determined system, the orthogonality condition

$$\sum_{j=1}^{N} w_j p(x_j)=0 \tag{16}$$

is further imposed on the coefficients $\mathbf{w}=(w_1,\ldots,w_N)$.

Let $P=(p_1,\ldots,p_l)$ be a basis for the polynomial and let $\mathbf{c}=(c_1,\ldots,c_l)$ be the coefficients that give P in terms of this basis. Then Equations (14) and (16) may be written in matrix form as

$$\begin{pmatrix} \mathbf{\Psi} & \mathbf{P} \\ \mathbf{P}^{\mathrm{T}} & 0 \end{pmatrix} \begin{pmatrix} w \\ c \end{pmatrix} = \begin{pmatrix} f \\ 0 \end{pmatrix} \tag{17}$$

where

$$\mathbf{\Psi}=\begin{pmatrix} \psi(0) & \psi(\|x_2-x_1\|) & \cdots & \psi(\|x_N-x_1\|) \\ \psi(\|x_1-x_2\|) & \psi(0) & \cdots & \psi(\|x_N-x_2\|) \\ \vdots & \vdots & \vdots & \vdots \\ \psi(\|x_1-x_N\|) & \psi(\|x_2-x_N\|) & \cdots & \psi(0) \end{pmatrix}$$

and $P_{i,j}=p_j(x_i),\ i=1,\ldots,N,\ j=1,\ldots,l$. Solving Equation (17) determines $\mathbf{c}$ and $\mathbf{w}$, hence $\tilde{f}(x)$.

2.2.3. Sampling methods. In the development of a meta-model, the location of sample points within the parametric space has an important influence on both the cost of constructing the model and on the accuracy of model predictions. In this work we have investigated the performance of two different sampling strategies; the full factorial and the Latin Hyper-Cube design-of-experiments.

The full factorial design-of-experiment uniformly samples the design parameters across the whole parameter space of interest. This technique while easy to implement is expensive requiring $\prod_{i=1}^{n} m_i+1$ samples where m_i is the number of intervals used to resolve the individual parameters and n is the number of parameters. This number can become excessively large for even a modest number of design parameters.

DOI: 10.1002/fld

In an effort to overcome the curse of dimensionality, a number of alternative sampling techniques have been proposed. In the Latin Hyper-Cube design sampling (LHS), each parameter range is divided into m intervals or bins of equal probability. This leads to a total of m^n bins in the whole space. Subsequently, m samples are generated such that for each parameter, when a one-dimensional projection is taken, there will be only one sample in each bin. The LHS algorithm produces samples as follows:

$$x_j^{(i)} = \frac{\pi_j^{(i)} + \kappa_j^{(i)}}{m} \quad \forall 1 \leqslant j \leqslant n, \;\; 1 \leqslant i \leqslant m \tag{18}$$

where m is the number of samples, $\kappa \in [0, 1]$ is a random number and π is an independent random number permutation. The subscript denotes the parameter number and the superscript in brackets denotes the sample number. From each parameter, one of the points on the interval is selected randomly and the response is evaluated. This is done until all points are used up. This method is useful because there is no correlation between parameters and the samples are chosen randomly. However, the space-filling characteristics produced using the standard LHS are not guaranteed to be optimal. In an effort to provide an optimal LHS design, the algorithm is modified using the approach of Audze and Englais [33]. In their approach a m^n grid is first generated and then the sample points are placed so that no two points lie along the same grid line and the metric,

$$\sum_{i=1}^{n} \sum_{j=i+1}^{n} \frac{1}{d_{ij}^2} \tag{19}$$

is minimized. In Equation (19) d_{ij} is the Euclidean distance between points i and j. In order to ensure that each point generated is placed in the centre of its bin, a lattice sampling technique is adopted in which the value of κ is set equal to 0.5.

3. RESULTS

The model developed in the preceding sections is demonstrated for the two aerodynamic problems presented in the introduction that are a flare-stabilized projectile and a fin-stabilized missile with nose control.

3.1. Flare-stabilized projectile

In this section the utility of POD as a means of obtaining reduced-order models is demonstrated using the example of inviscid steady flow about an axi-symmetric flare-stabilized projectile. For this case parametric variation of both flow condition (Mach number) and geometry (flare base radius) were considered. The Mach number range [4.0, 6.0] was divided into 20 uniform intervals, while the non-dimensionalized flare base radius r/D range [0.75, 1.25] was divided into 10 uniform intervals. The full factorial design-of-experiment was employed to generate the sample points resulting in an ensemble containing a total of 231 snapshots.

Figure 1 shows the geometry of the projectile with maximum and minimum flare angles, while Figure 2 shows an example of the grid on which the axi-symmetric inviscid computations were performed.

DOI: 10.1002/fld

Figure 1. Geometry of the axi-symmetric projectile: (a) $r/D=1.25$ and (b) $r/D=0.75$.

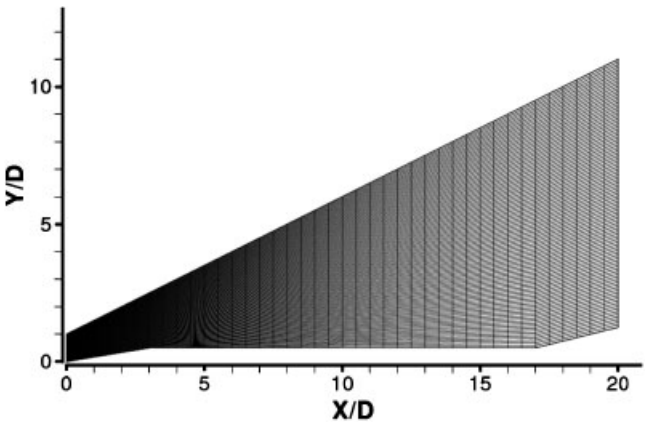

Figure 2. Two-dimensional grid with 41×101 grid points used for the Euler computations at $r/D=1.25$.

3.1.1. Reduced-order modelling. The POD method was applied to the resulting data set and a model containing 231 basis vectors was obtained. This model was used to reconstruct the solution at a Mach number of 4.0 and a flare base radius of r/D = 0.75. The results are summarized in Figures 3–5. Figure 3 shows the variation of the energy defined in Equation (11) captured by the POD modes for each of the primitive variables against the number of POD modes. It is evident that most of the energy (99.9%) is captured within the first few modes, indicating that the data set is rich enough to capture the flow details.

While the energy captured by a given set of basis functions provides some understanding of the relative accuracy of the model, the actual error remains unknown. This quantity can be quantified by comparing the original sample data with that generated by the reduced-order model. In this example an assessment is made by determining the percentage variation of the root mean square value of the global error in the whole flow field for each of the primitive variables as it varies with the number of POD modes. The biggest error was registered by the cross-flow v-velocity. For this case the percentage root mean square global error in the whole flow field reduces to approximately 0.1% when using only 60 of the 231 available POD modes (Figure 4).

Figure 5 illustrates this more clearly by comparing static pressure contours obtained from the reduced-order model using 1, 15 and 35 POD modes with those of the original Euler computation. A comparison of the normalized static pressure distribution at the outflow is also included. The

DOI: 10.1002/fld

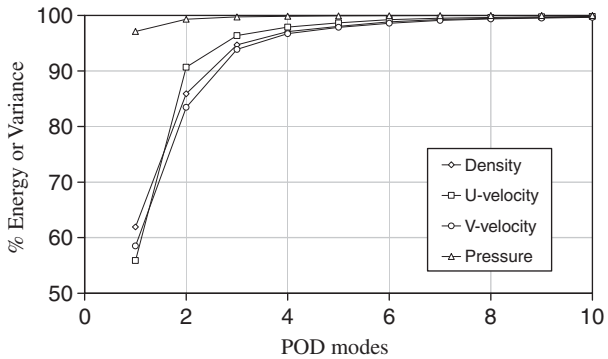

Figure 3. Percentage energy captured for each of the primitive variables versus the number of POD modes.

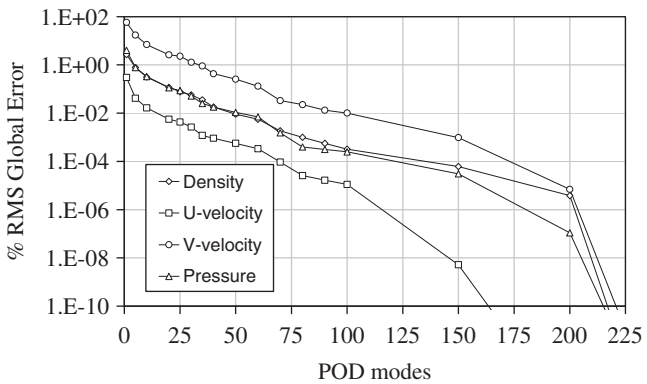

Figure 4. Global RMS % Error for each of the primitive variables versus the number of POD modes.

static pressure is normalized by the free-stream pressure. Using a single POD mode, the main flow features, the conical shock at the nose and the compression over the flare, are reasonably represented though there is significant disagreement in the outflow pressure distribution. For one single POD mode, the RMS global error in the whole static pressure flow field is 4.0%. With 15 modes considerable improvements are obtained. The conical shock is now essentially identical to that of the Euler computation, while the detail of the compression is much better represented than with just one mode. In this case, small discrepancies are noticeable in the pressure distribution at the outflow. Further improvements are obtained with 35 POD modes, where the entire flow field is now essentially identical to that obtained by solution of the Euler equations. This is also evident from the outflow pressure distribution. The RMS global error within the whole static pressure field is 0.03%.

A useful application of this technique is that of data compression. This is achieved by keeping the most energetic POD modes while neglecting the rest without much loss of detail. Figure 6 shows pictorially this potential by making a direct comparison between the percentage RMS global error in the cross-flow v-velocity field and the percentage effective data in use versus the number of POD modes. With the consideration of only 10 POD modes and hence only 4.4% of the total

DOI: 10.1002/fld

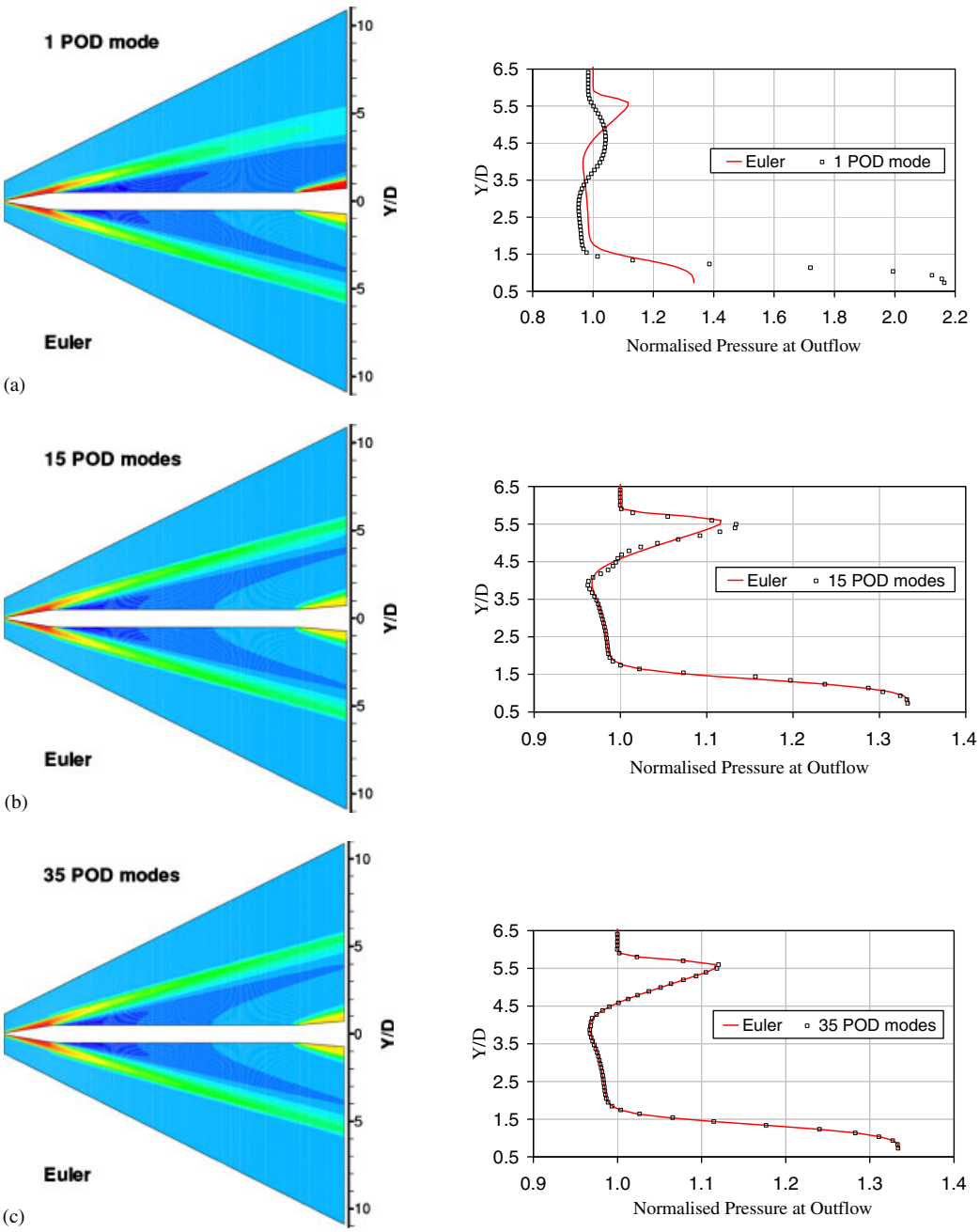

Figure 5. Comparison of pressure contours at $M=4.0$ and $r/D=0.75$ obtained using the meta-model (upper) and Euler computation (lower): (a) 1 POD mode; (b) 15 POD modes; and (c) 35 POD modes.

DOI: 10.1002/fld

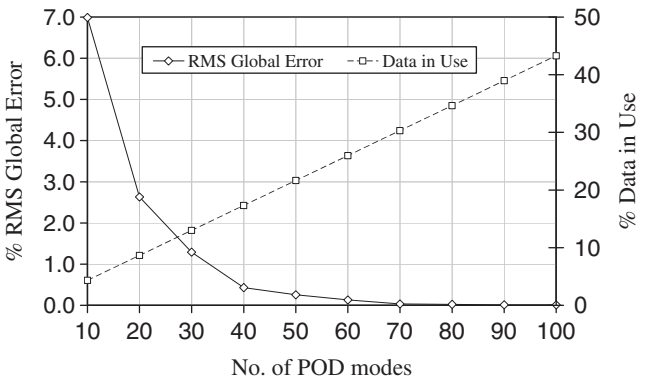

Figure 6. Percentage of RMS Global Error in the cross-flow velocity and percentage of data in use versus number of POD modes.

amount of data, the global RMS error in the cross-flow velocity field is 7.0%. By considering 100 POD modes and therefore using 43.4% of the total data, the RMS global error in the cross-flow v-velocity field goes down to 0.01%. This shows that by using 43.4% of the data only, the solutions can be reconstructed with very high accuracy. Thus, this methodology offers an effective and valuable data management system for both data storage and handling by compressing the data.

3.1.2. Model predictions. Having established that the reduced-order model provides good means for data reconstruction, attention was then directed to making model predictions. The scalar coefficients obtained from the data ensemble used in the previous example were used together with cubic splines to generate an interpolated response surface. The resulting model provides a basis for computing the flow field at any Mach number and flare base radius encompassed within the sampled space, but not co-incident with the generating data set parameters.

Figure 7 presents comparisons of the predicted pressure field contours with the Euler computation for a Mach number of 5.37 and a base radius of $r/D=1.25$. The interpolation in this example is one-dimensional, that is along the Mach numbers within the Mach number range as data exist at this base radius. For this example, the behaviour with increasing number of POD modes is similar to that of the previous case, with as few as 15 POD modes a reasonable representation of the main flow features can be obtained, while increasing the number of POD modes leads to successive improvements in the detail of the captured pressure variation. For this case, with 71 of the 231 available POD modes resulted in a global RMS error in the pressure field of 0.012% when compared with the high-fidelity solution. This compares with a typical global RMS error in the pressure field of 0.0025% when the model is used to reconstruct a snapshot from the data set of observations. Predictions in both parameters show similar behaviour. For a Mach number of 4.87 and a base flare radius of $r/D=1.03$, the use of 71 POD modes resulted in a global RMS error between the POD model-predicted and Euler-computed pressure fields of 0.016%.

For the latter case, the influence of the number of samples in the initial ensemble on the model predictions was also investigated. PODs employing 21, 11 and 5 samples at equal intervals to discretize the Mach number range, corresponding to 231, 121 and 55 snapshots, respectively, were studied. In an effort to isolate the effects of sample size, it was ensured that the predictions obtained for individual ensembles were independent of the number of modes in the reduced model. This

DOI: 10.1002/fld

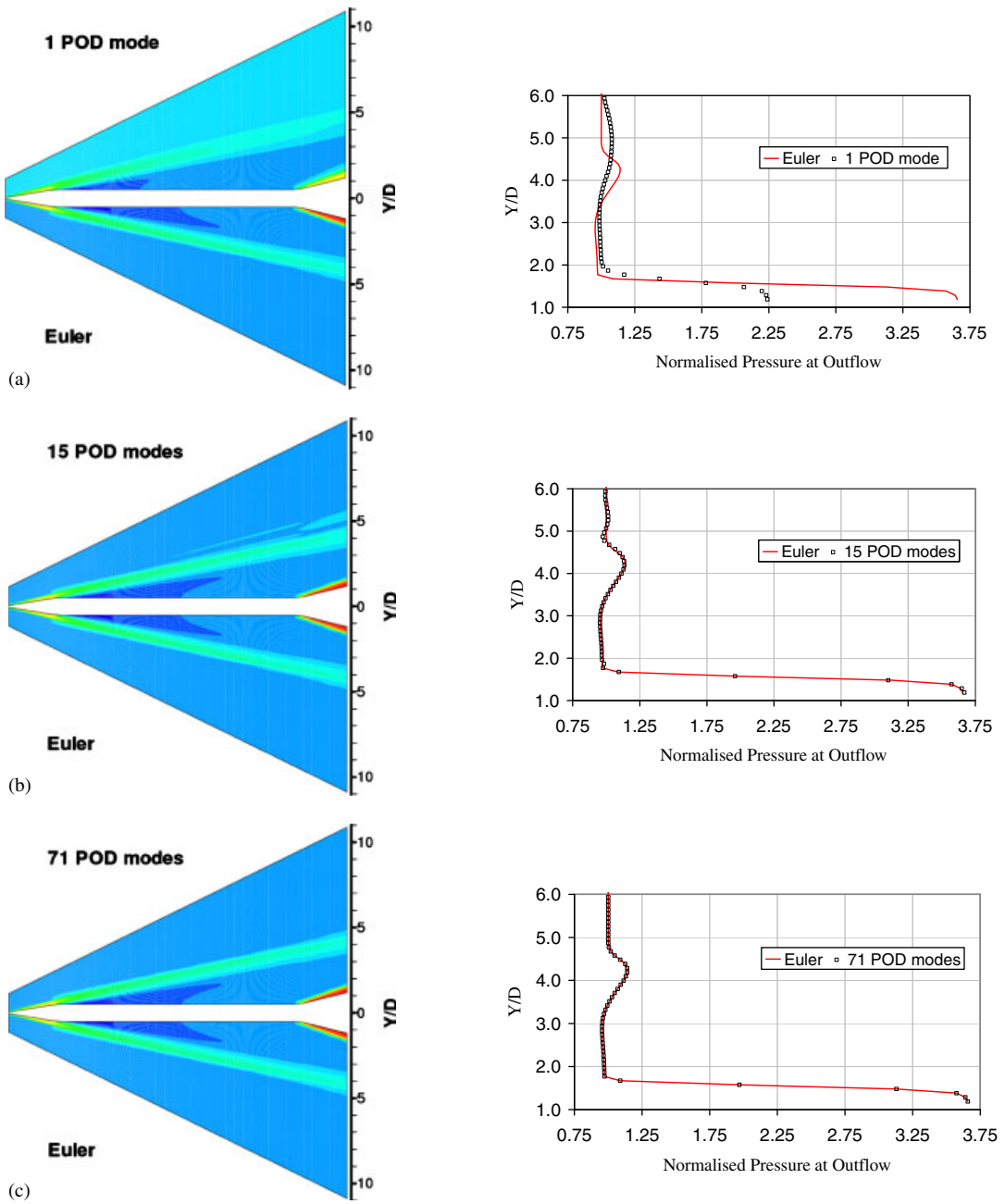

Figure 7. Comparison of pressure contours at $M = 5.37$ and $r/D = 1.25$ obtained using the meta-model (upper) and Euler computation (lower): (a) 1 POD mode; (b) 15 POD modes; and (c) 71 POD modes.

DOI: 10.1002/fld

was typically obtained using 40% of the available POD modes. A strong relationship between the sample size and error was found. For the smallest ensemble with 55 snapshots, the global RMS error in the pressure field was found to be 0.68%, while for 121 and 231 snapshots the error reduced to 0.15 and 0.016%, respectively.

3.1.3. Model predictions for three-dimensional flow. In an effort to understand more clearly the relationship between the model prediction and the method used to obtain a pseudo-continuous representation of the scalar coefficients, a second study was undertaken. For this case the parameters of interest were extended to include incidence. The Mach number range [4.0, 6.0] was divided into 4 uniform intervals instead of the 20 used in the previous axi-symmetric study; the incidence range $[0.0^\circ, 4.0^\circ]$ was also divided into 4 uniform intervals and the flare base radius range $[r/D{=}0.8, r/D = 1.2]$ was divided using a further 4 intervals, instead of the 10 intervals used previously. The observations in this case were sampled according to a full factorial design-of-experiment requiring a total of 125 evaluations of the IMPNS analysis code.

Predictions were made at two points in the parameter space, a point towards the centre of the space ($\alpha = 2.2^\circ$, $M = 5.3$, $r/D = 1.05$) and a point close to the boundary of the sampled space ($\alpha = 0.7^\circ$, $M = 4.2$, $r/D = 0.85$). In both cases none of the parameters of interest correspond to values used to generate the ensemble of snapshots. The predictions obtained for each of the modelling approaches (linear regression, linear spline interpolation, cubic spline interpolation and a polynomial augmented multi-quadric RBF) are summarized in Table I. In this table, forces and moments are presented that have been obtained by integrating the predicted surface pressures. The reduced-order model used 40 out of the 125 available POD modes; increasing this number had no significant effect on the predicted values.

The results suggest that of the methods considered, the response surface constructed using a polynomial-augmented multi-quadric RBF is most effective. Surprisingly the linear regression, which employs quadratic polynomials, performs no better than the linear spline interpolation. This is attributed to the global nature of the regression analysis used to obtain the response surface that appears to excessively smooth the computed coefficients. As the interpolation schemes pass through the supporting data exactly, they provide a much better representation of local variations in the data.

To confirm this hypothesis, the effects of data locality on the predictions obtained from the linear regression-based model were investigated. In this case the parameters' range was reduced in size as shown in Table II. Each parameters' range was discretized using two equal intervals resulting in a total ensemble of 27 snapshots. By successively localizing the data-improved predictions were obtained. This behaviour is attributed to improved representation of the local parametric variations by the response surface rather than improvements in the reduced-order model.

3.1.4. Latin hyper-cube sampling. The use of parameter sampling techniques based upon the full factorial design-of-experiment can be prohibitively expensive for problems involving large numbers of parameters. To overcome this problem, sampling techniques based upon Latin Hyper-Cube sampling were explored. In this approach a given number of samples are distributed in an optimal manner within the parameter space, see Vavalle [1] for a more detailed discussion. Table III presents results obtained using the Latin Hyper-Cube sampling. For this example the parameter space considered was that with an angle of attack varying between $[1^\circ, 3^\circ]$, a Mach number between [5.0, 6.0] and a base flare radius r/D between 0.9 and 1.1. The parameter space was populated using only 27 snapshots. Despite the limited number of snapshots considered, the achieved accuracy

DOI: 10.1002/fld

Table I. Comparison of model predictions with CFD simulations with various modelling strategies.

	$\alpha=2.2^\circ,\ M=5.3,\ r/D=1.05$			$\alpha=0.7^\circ,\ M=4.2,\ r/D=0.85$		
	Meta-model	CFD	% Error	Meta-model	CFD	% Error
Linear regression						
C_x	0.3518	0.3536	0.51	0.1670	0.1658	0.72
C_z	0.2591	0.2580	0.43	0.0566	0.0570	0.70
C_m	−2.7795	−2.7709	0.31	−0.4714	−0.4557	3.45
X_{cp}	10.7257	10.7414	0.15	8.3290	7.9985	4.13
Linear spline interpolation						
C_x	0.3573	0.3536	1.05	0.1694	0.1658	2.17
C_z	0.2594	0.2580	0.54	0.0575	0.0570	0.88
C_m	−2.7897	−2.7709	0.67	−0.4658	−0.4557	2.22
X_{cp}	10.7559	10.7414	0.13	8.1002	7.9985	1.27
Cubic spline interpolation						
C_x	0.3526	0.3536	0.28	0.1682	0.1658	1.45
C_z	0.2575	0.2580	0.19	0.0572	0.0570	0.35
C_m	−2.7644	−2.7709	0.23	−0.4616	−0.4557	1.29
X_{cp}	10.7345	10.7414	0.06	8.0715	7.9985	0.91
Polynomial augmented multi-quadric RBF						
C_x	0.3537	0.3536	0.03	0.1660	0.1658	0.12
C_z	0.2579	0.2580	0.04	0.0570	0.0570	0.00
C_m	−2.7702	−2.7709	0.03	−0.4570	−0.4557	0.29
X_{cp}	10.7402	10.7414	0.01	8.0197	7.9985	0.27

Table II. Effect of data localization on model predictions.

		$\alpha=2.2^\circ,\ M=5.3,\ r/D=1.05$		
Parameters' range		Meta-model	CFD	% Error
$\alpha=[2^\circ,4^\circ],\ M=[5,6],\ r/D=[0.9D,1.1D]$	C_x	0.3542	0.3536	0.17
	C_z	0.2556	0.2580	0.93
	C_m	−2.7266	−2.7709	1.60
	X_{cp}	10.6681	10.7414	0.68
$\alpha=[2^\circ,4^\circ],\ M=[5,6],\ r/D=[1.0D,1.1D]$	C_x	0.3540	0.3536	0.11
	C_z	0.2563	0.2580	0.66
	C_m	−2.7395	−2.7709	1.13
	X_{cp}	10.6901	10.7414	0.48
$\alpha=[1^\circ,3^\circ],\ M=[5,6],\ r/D=[1.0D,1.1D]$	C_x	0.3540	0.3536	0.11
	C_z	0.2575	0.2580	0.19
	C_m	−2.7611	−2.7709	0.35
	X_{cp}	10.7230	10.7414	0.17

is better than that obtained for the examples presented earlier that used many more or the same number of snapshots. This is evident from both response surface construction methods utilized in this section. The prediction obtained from the polynomial-augmented multi-quadric RBF is highly accurate.

For this particular example a meta-model of the individual-integrated forces, pitching moment and centre of pressure was also developed by generating response surfaces for each property using

DOI: 10.1002/fld

Table III. Comparison of model predictions with CFD computations using the Latin Hyper-Cube Sampling technique.

	$\alpha=2.2,\ M=5.3,\ r/D=1.05$		
	Model	CFD	% Error
Linear regression			
C_x	0.3538	0.3536	0.06
C_z	0.2577	0.2580	0.12
C_m	−2.7647	−2.7709	0.22
X_{cp}	10.7281	10.7414	0.12
Polynomial augmented multi-quadric RBF			
C_x	0.3536	0.3536	0.00
C_z	0.2581	0.2580	0.04
C_m	−2.7722	−2.7709	0.05
X_{cp}	10.7404	10.7414	0.01

Table IV. Comparison of an RSM-based meta-model for the forces and moments with CFD computations.

	$\alpha=2.2,\ M=5.3,\ r/D=1.05$		
	Predicted	CFD	% Error
Linear regression			
C_x	0.3536	0.3536	0.00
C_z	0.2577	0.2580	0.12
C_m	−2.7645	−2.7709	0.23
X_{cp}	10.7282	10.7414	0.12

linear regression. This model was used to predict the forces, moment and centre of pressure at the previous point. A comparison with computed data is presented in Table IV.

From Tables III and IV, it is evident that the two regression methods provide results that are almost identical. While the evaluation of forces and moments from a meta-model of the individual-integrated forces and moment data is less expensive than from the POD model based on the full CFD output, the resulting information is limited to that in the model. In the case of the POD model, any result that can be deduced from the CFD data can now be also deduced from the POD model. This represents a significant advantage in many practical design situations.

From this section one can remark that the POD offers an effective reduced-order modelling methodology. In addition when coupled with interpolation or regression methods, it provides a very efficient means for making predictions. Interpolation-based response surface construction methods provide a better representation of the local parametric variations, though local regression methods provide improved representations than the global ones. Moreover the use of optimized sampling techniques for populating the parametric space such as the LHS provides a practical approach to reduce the number of samples required while achieving an improved accuracy.

DOI: 10.1002/fld

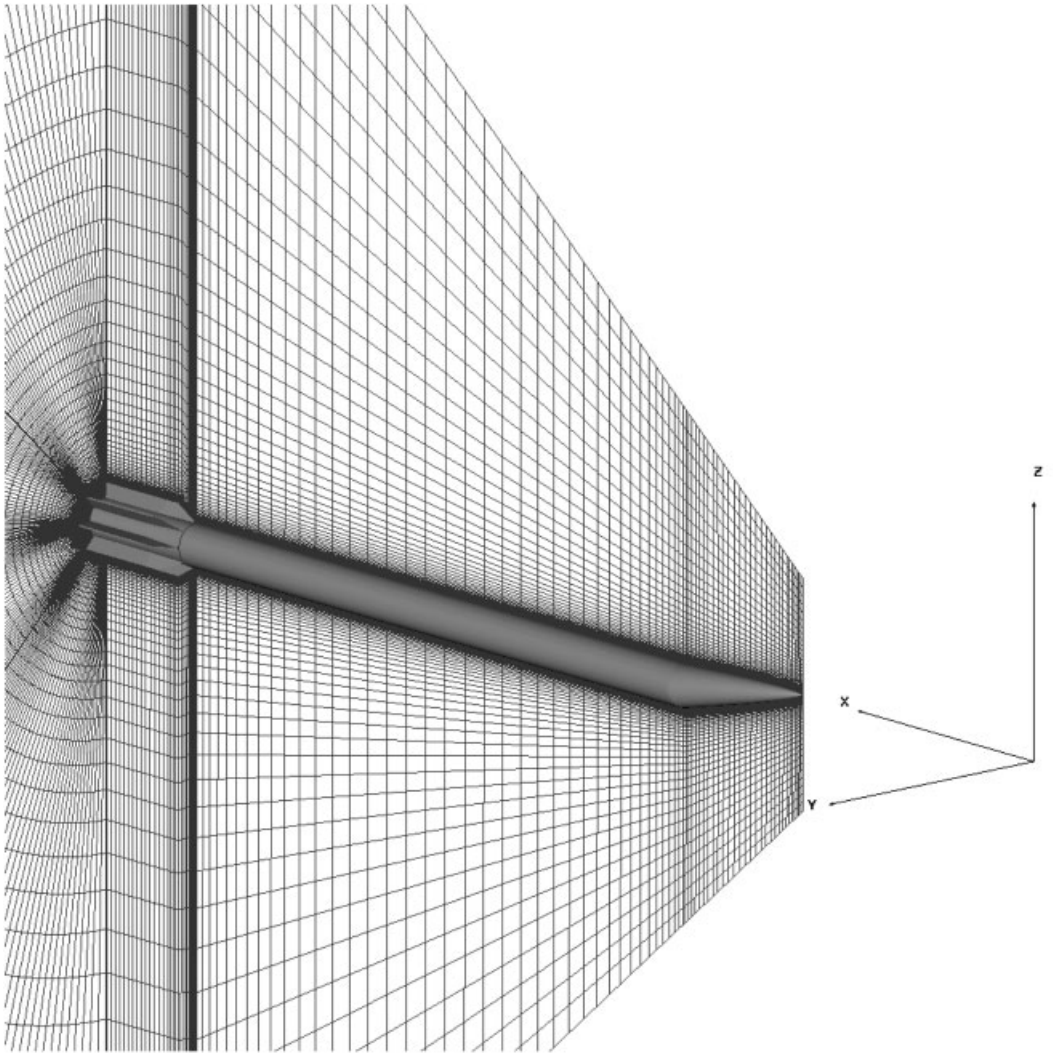

Figure 8. Nose controlled weapon configuration with a nose deflection of 8° and the computational grid with approx. 1 million grid points.

3.2. Fin-stabilized projectile with drooping nose control

The second problem considered in the current study relates to supersonic turbulent flow around a realistic weapon configuration. The configuration consists of a 0.7 power series nose followed by a cylindrical body with eight stabilizing fins. The nose is free to rotate in the pitch plane, providing a means of control. Figure 8 presents a visualization of the geometry and a typical grid for a nose deflection of 8°. Two parameters, the nose deflection and the flow angle of attack were varied. The nose deflection was allowed to vary in the range $[0°, 8°]$, while the flow angle of attack was varied in the range $[0°, 6°]$. In this case a full factorial design-of-experiment was used to sample

DOI: 10.1002/fld

Table V. Comparison of model predictions with CFD simulations for $\delta=5°$ and $\alpha=1°,\ \alpha=3°,\ \alpha=5°$.

	$\delta=5°$								
	$\alpha=1°$			$\alpha=3°$			$\alpha=5°$		
	Model	CFD	% Error	Model	CFD	% Error	Model	CFD	% Error
CSI									
C_x	0.1864	0.1868	0.21	0.1904	0.1934	1.55	0.2034	0.2044	0.49
C_z	0.1944	0.1916	1.46	0.5040	0.5048	0.16	0.9262	0.9191	0.77
C_m	−1.497	−1.491	0.40	−5.755	−5.717	0.66	−11.320	−11.261	0.53
X_{cp}	7.701	7.779	1.01	11.419	11.324	0.84	12.222	12.252	0.25
Tri-harmonic RBF									
C_x	0.1853	0.1868	0.80	0.1860	0.1934	3.83	0.2029	0.2044	0.73
C_z	0.1921	0.1916	0.26	0.5035	0.5048	0.26	0.9189	0.9191	0.02
C_m	−1.451	−1.491	2.68	−5.752	−5.717	0.61	−11.243	−11.261	0.16
X_{cp}	7.553	7.779	2.92	11.424	11.324	0.89	12.235	12.252	0.14

the parameter space. The Latin-Hyper-Cube sampling technique was not used in this case as this would have entailed the generation of a new grid, each time the nose deflection is changed. All of the computations were performed with an inflow Mach number of 3.0, a free-stream static temperature of 110°K and a Reynolds number of 9.5 million per foot.

3.2.1. Model predictions. For the first prediction a subset of the available data was employed. The nose deflection was varied in the range $[2°, 8°]$, while angle of attack was varied between $[0°, 6°]$; uniform intervals of 2° were used for both parameters. A POD was performed on the ensemble of computational experiments. In this example all 16 of the available POD modes were utilized and pseudo-continuous models were obtained using cubic-spline interpolation and a tri-harmonic RBF. These two modelling methods were used as they offered good generalization ability. Predictions are compared with high-fidelity simulations in Table V for a nose deflection of 5° at an angle of attack of 1°, 3° and 5°. The comparisons are considered to be acceptable given the small number of modes available within the POD.

As seen before, improving the locality of the data results in slightly improved predictions, although in this case it is thought that the errors arise principally as a consequence of grid deformation. This can be seen in Table VI in which predictions obtained from an ensemble with the nose deflection varying between $[4°, 6°]$ in intervals of 1° and an angle of attack varying between $[0°, 6°]$ in intervals of 2° are compared with CFD simulations. In addition to the previously mentioned two interpolating techniques, a Gaussian kernel was considered as well. A comparison between the results obtained by the cubic splines and the Gaussian RBF shows that indeed the cubic splines provide a good generalization ability in this problem.

Improving the resolution of incidence α from 2° to 1° intervals provides further improvements in the predicted data, Table VII. Tables V, VI and VII show that the cubic spline interpolation and the tri-harmonic RBF are of comparable accuracy as expected, since the tri-harmonic RBF is, in fact, a cubic spline. These results suggest that by using suitable kernels in a generalized linear model, it is possible to approximate any function to an arbitrary degree of accuracy. Figure 9 compares the axial pressure and density distributions obtained from the meta-model with CFD simulations

DOI: 10.1002/fld

Table VI. Comparison of model predictions with CFD simulations due to improved data locality, $\delta=5^\circ$ and $\alpha=1^\circ,\ \alpha=3^\circ,\ \alpha=5^\circ$.

	$\delta=5^\circ$								
	$\alpha=1^\circ$			$\alpha=3^\circ$			$\alpha=5^\circ$		
	Model	CFD	% Error	Model	CFD	% Error	Model	CFD	% Error
CSI									
C_x	0.1881	0.1868	0.70	0.1918	0.1934	0.83	0.2051	0.2044	0.34
C_z	0.1941	0.1916	1.30	0.5041	0.5048	0.14	0.9278	0.9191	0.95
C_m	−1.486	−1.491	0.30	−5.747	−5.717	0.54	−11.324	−11.261	0.56
X_{cp}	7.660	7.779	1.54	11.401	11.324	0.68	12.205	12.252	0.38
Tri-harmonic RBF									
C_{x}	0.1906	0.1868	2.03	0.1894	0.1934	2.07	0.2087	0.2044	2.10
C_z	0.1961	0.1916	2.35	0.5033	0.5048	0.30	0.9236	0.9191	0.49
C_m	−1.497	−1.491	0.38	−5.739	−5.717	0.38	−11.286	−11.261	0.22
X_{cp}	7.630	7.779	1.92	11.403	11.324	0.70	12.2185	12.2517	0.27
Gaussian RBF									
C_x	0.1898	0.1868	1.61	0.1911	0.1934	1.19	0.2058	0.2044	0.68
C_z	0.1923	0.1916	0.37	0.5043	0.5048	0.10	0.9212	0.9191	0.23
C_m	−1.431	−1.491	4.00	−5.750	−5.717	0.59	−11.282	−11.261	0.19
X_{cp}	7.441	7.780	4.37	11.402	11.324	0.68	12.247	12.252	0.04

Table VII. Comparison of model predictions with CFD simulations, $\delta=5^\circ$ and $\alpha=2.5^\circ$.

	$\alpha=2.5^\circ,\ \delta=5^\circ$		
	Model	CFD	% Error
CSI			
C_x	0.1901	0.1904	0.16
C_z	0.4160	0.4162	0.05
C_m	−4.5013	−4.5072	0.13
X_{cp}	10.8197	10.8293	0.09
Tri-harmonic RBF			
C_x	0.1901	0.1904	0.16
C_z	0.4159	0.4162	0.07
C_m	−4.5003	−4.5072	0.15
X_{cp}	10.8212	10.8293	0.07
Gaussian RBF			
C_x	0.1901	0.1904	0.16
C_z	0.4161	0.4162	0.02
C_m	−4.5074	−4.5072	0.00
X_{cp}	10.8316	10.8293	0.02

at 0° and 180° azimuth angles. The agreement is generally excellent with the exception of the shock intensity at the fin.

Figure 10 compares the circumferential pressure distributions at stations located 1, 3 and 10.5 calibres downstream of the nose. The agreement is generally good over most of the body, but some small discrepancies are observed in the secondary flow separation and re-attachment at 10.5

DOI: 10.1002/fld

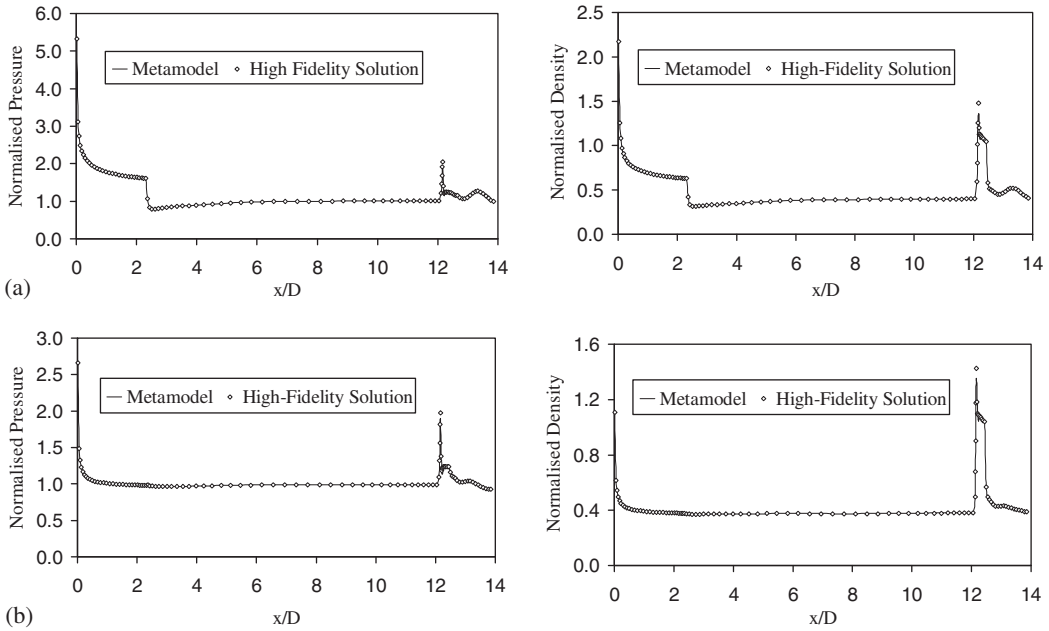

Figure 9. Comparison of predicted axial distribution of pressure and density with CFD simulations, $\delta = 5°$ and $\alpha = 2.5°$: (a) Windward and (b) Leeward.

calibres (Figure 10(d)). In Figure 11 predicted density contours are compared with CFD simulations at two stream-wise locations. The first is located well downstream of the nose cylinder junction, while the second is located at the trailing edge of the fins. This figure, together with Table VII and Figures 9 and 10, suggests that the model provides an acceptable surrogate for the IMPNS flow solver and illustrates the potential of the method. In this particular case the full CFD output from the meta-model is obtained in 107 s of CPU time on a 3.3 GHz processor. This compares favourably to the 18 000 s of CPU time necessary for making one complete evaluation using the CFD code. In case the CFD code is a time-marching one, the difference in CPU time would be considerably higher. Consequently the meta-model becomes much more useful. In such case the output from the meta-model could also be used to restart the computation and hence it would assist in reducing the overall computational time of the CFD code.

4. CONCLUSIONS

A high-fidelity, low-cost aerodynamic model was presented for use in parametric studies of weapon aerodynamics. The method employs a reduced-order model obtained from the POD of an ensemble of CFD solutions. It has been shown that this procedure provides a data compression methodology by retaining the most energetic modes while discarding the rest without any significant loss of detail. Moreover, by using generalized linear models for a pseudo-continuous representation of the projection coefficients describing the reduced-order model, predictions of parameter combinations not in the original set of observations are made.

DOI: 10.1002/fld

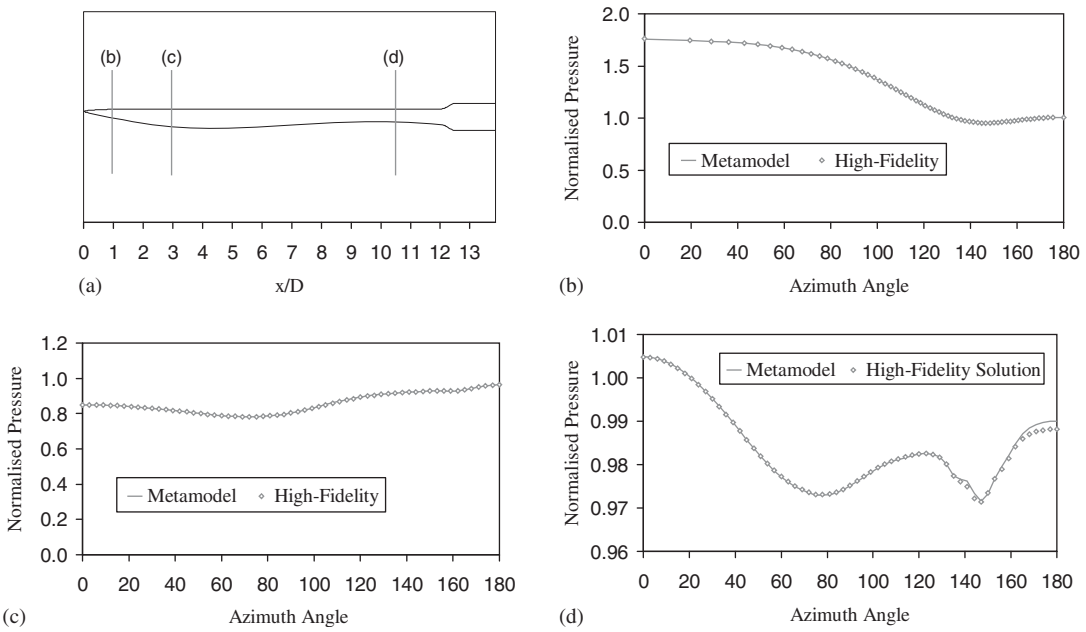

Figure 10. (a) Body geometry and streamwise locations; (b) (c) (d) circumferential normalized pressure distributions at $\delta = 5^\circ$ and $\alpha = 2.5^\circ$ ((b) $x/D = 1.0$; (c) $x/D = 3.0$; and (d) $x/D = 10.5$).

Four different approaches to the construction of a response surface of the projection coefficients were investigated, a linear regression-based method and three interpolation techniques employing linear spline, cubic spline and RBFs. The computed data suggest that interpolation-based techniques provide a significant advantage over the regression method. This is attributed to the fact that the interpolation schemes pass through all of the sample points providing an improved representation of local minima and maxima, while the global fit of the regression technique produces some unnecessary smoothing. This observation is supported by studies of data localization that suggest the regression method can provide similar accuracy to the interpolation schemes when employed over a reduced parameter space. In general, the RBF interpolation offered the most accurate prediction.

The use of Latin Hyper-Cube sampling methods was found to offer improved accuracy for a given number of sample points. For problems involving large numbers of parameters, the LHS may provide a practical approach to reduce the number of samples required to populate the design space. However, for problems involving geometric variation the LHS requires a means of automatically generating high-quality grids. For this reason a more practical tool may incorporate a hybrid approach, a design-of-experiment technique in which the geometry variables are prescribed at specific levels, and an LHS technique that is used for other parameters.

The results of the study suggest that meta-models based upon POD of a small number of computational experiments can provide a reliable low-cost high-fidelity tool. In contrast to many of the modelling efforts reported in the literature, this model provides access to the full CFD output. The current approach requires 107 s of CPU time on a 3.3 GHz processor to compute the model and make a single prediction; this compares favourably to the 18 000 s required for one evaluation of the CFD code.

DOI: 10.1002/fld

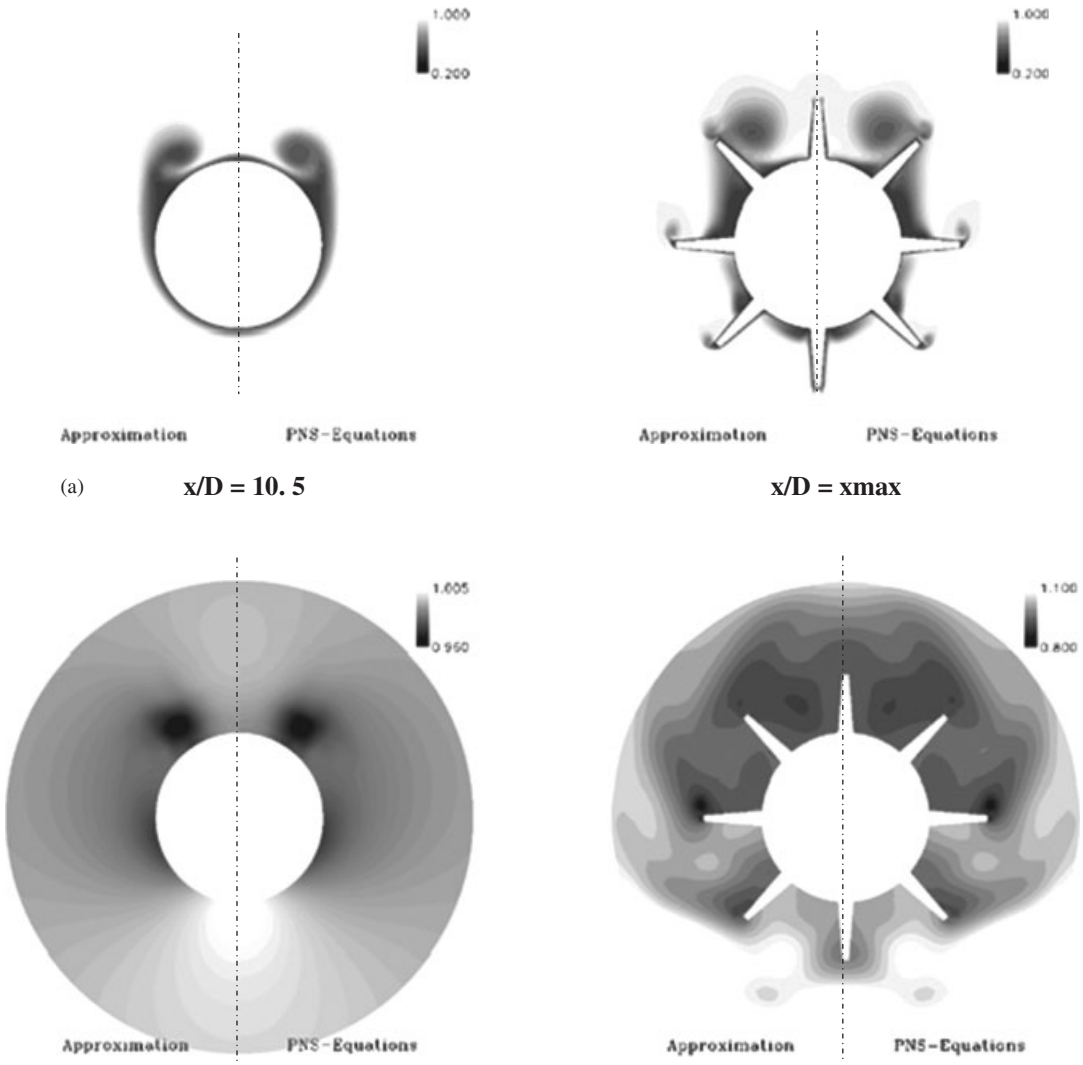

Figure 11. Comparison of pressure and density contours, $\delta = 5°$ and $\alpha = 2.5°$: (a) density contours (left—meta-model, right—Navier–Stokes) and (b) pressure contours (left—meta-model, right—Navier–Stokes).

DOI: 10.1002/fld

NOMENCLATURE

α_{ij}	is the scalar or projection coefficient of the jth POD mode
Φ_{ij}	is the jth POD basis mode
m	is the number of realizations or snapshots and POD modes
n	is the number of grid points in a mesh
$\mathbf{x}$	is a vector of different parameter values
$\mathbf{Y}$	is a solution vector of primitive or conservative variables
$f(x)$	computationally expensive analysis
$\tilde{f}(x)$	approximation to $f(x)$
r	radial distance from a given centre point
$\Psi(r)$	a typical RBF
$p(x)$	a polynomial of one degree less than the RBF $\Psi(r)$
α	angle of incidence
δ	nose deflection angle of the nose-controlled missile configuration
D	mid-body diameter
M	Mach number
C_x	component of the aerodynamic force along the axis of the body
C_z	component of the aerodynamic force normal to the axis of the body
C_m	pitching moment acting on the body
X_{cp}	centre of pressure coordinate along the body axis

ACKNOWLEDGEMENTS

This work has been funded by the Defence Science and Technology Laboratory (DSTL). The authors would like to thank Trevor Birch of DSTL for the useful discussions conducted during the development of this work. The IMPNS software was developed with the financial support of DSTL and QinetiQ Ltd.

REFERENCES

1. Vavalle A. Response surface aerodynamic optimisation for blended wing body aircraft. *Ph.D. Thesis*, Cranfield University, 2005.
2. Holmes P, Lumley J, Berkooz G. *Turbulence*, *Coherent Structures*, *Dynamical Systems and Symmetry*. Cambridge University Press: Cambridge, U.K., 1996.
3. Schmidt E, Held B, Savick D. Hypervelocity launch dynamics. *AIAA 93-0502*, *31st Aerospace Sciences Meeting and Exhibit*, Reno, NV, 1993.
4. Plostins P, Silton S, Schmidt E, Soencksen K. Aerodyanamic jump at hypervelocity. *AIAA 2005-438*, *43rd AIAA Aerospace Sciences Meeting and Exhibit*, Reno, NV, 2005.
5. Landers MG, Hall LE, Auman LM, Vaughn ME. Deflectable nose and canard controls for a fin-stabilized projectile at supersonic and hypersonic speeds. *AIAA 2003-3805*, *21st Applied Aerodynamics Conference*, Orlando, FL, 2003.
6. Shoesmith B, Birch T, Mifsud M, Meunier M, Shaw S. CFD analysis of a supersonic projectile with deflectable nose control. *AIAA 2006-3200*, *Third AIAA Flow Control Conference*, San Francisco, CA, 2006.
7. Ludlow DK. IMPNS user's manual. *CoA Report NFP-0113*, Cranfield University, 2001.
8. Ludlow DK. IMPNS theory guide. *CoA Report NFP-0112*, Cranfield Univesity, 2001.
9. Baldwin B, Lomax H. Thin layer approximation and algebraic model for separated turbulent flow. *AIAA 78-257*, 1978.
10. Degani D, Schiff LB. Computation of turbulent supersonic flows around pointed bodies having cross-flow separation. *Journal of Computational Physics* 1986; **66**(3):173–196.

DOI: 10.1002/fld

11. Qin N, Jayatunga C. Algebraic turbulence modelling for vortical flows around slender bodies. *NATO RTO-MP-5*, Missile Aerodynamics, Paper 20, 1998.
12. Spalart PR, Allmaras SR. A one-equation turbulence model for aerodynamic flow. *AIAA 92-0439*, 1992.
13. Wilcox DC. *Turbulence Modeling for CFD* (2nd edn). DCW Industries Inc.: La Canada, CA, U.S.A., 1998.
14. Qin N, Ludlow DK. A cure for anomalies of Osher and AUSM+ schemes for hypersonic viscous flows around swept cylinders. In *Proceedings of the 22nd International Symposium on Shock Waves*, Ball GJ, Hillier R, Hoberts GT (eds). Imperial College: London, U.K., 1999; 635–640.
15. Osher S, Solomon F. Upwind difference schemes for hyperbolic systems of conservative laws. *Mathematics of Computation* 1992; **38**(1):339–374.
16. Shaw S, Qin N. A matrix-free preconditioned Krylov subspace method for the PNS equations. *AIAA 98-111*, 1998.
17. Qin N, Ludlow DK, Zhong B, Shaw ST, Birch TJ. Multigrid acceleration of a preconditioned GMRES implicit PNS solver. *AIAA 99-0779*, 1999.
18. Saad Y, Schultz MH. GMRES: a generalised minimal residual algorithm for solving non-symmetric linear systems. *SIAM Journal on Scientific and Statistical Computing* 1986; **7**:856–869.
19. Brandt A. Multi-level adaptive solutions to boundary-value problems. *Mathematics of Computation* 1977; **31**: 333–390.
20. Qin N, Richards BE. Finite volume 3DNS and PNS solutions of hypersonic viscous flows around a delta wing using Osher's flux difference splitting. *Proceedings of a Workshop on Hypersonic Flows for Re-entry Problems*, Berlin, 1990.
21. Birch TJ, Ludlow DK, Qin N. Towards an efficient, robust and accurate solver for supersonic viscous flows. *Proceedings of the ICAS 2000 Congress*, Harrogate, U.K., 2000.
22. Birch TJ, Prince SA, Ludlow DK, Qin N. The application of a parabolized Navier–Stokes solver to some hypersonic flow problems. *AIAA 2001-1753*, 2001.
23. Birch TJ, Qin N, Jin X. Computation of supersonic viscous flows around a slender body at incidence. *AIAA 94-1938*, 1994.
24. Mifsud MJ, Shaw ST. Credible CFD simulations of complex supersonic weapon configurations using the IMPNS software. *CCA Report 2005-02*, Centre for Computational Aerodynamics, Department of Aerospace Science, School of Engineering, Cranfield University, 2005.
25. Lumley JL. The structure of inhomogenous turbulence. In *Atmospheric Turbulence and Wave Propagation*, Yaglom AM, Tatarski VI (eds). Nauka: Moscow, 1967; 166–178.
26. Epureanu BI, Dowell EH, Hall K. A parametric analysis of reduced order models of potential flows in turbomachinery using proper orthogonal decomposition. *2001-GT-0434*, *Proceedings of ASME TURBO EXPO 2001*, New Orleans, LA, 2001.
27. LeGresley P, Alonso J. Investigation of non-linear projection for POD based reduced order models for aerodynamics. *AIAA 2001-0926, 39th Aerospace Sciences Meeting and Exhibit*, Reno, NV, 2001.
28. Bui-Thanh T, Damodaran M, Willcox K. Proper orthogonal decomposition extensions for parametric applications in compressible aerodynamics. *AIAA 2003-4213*, *21st Applied Aerodynamics Conference*, Orlando, FL, 2003.
29. Kirby M, Boris JP, Sirovich L. A proper orthogonal decomposition of a simulated supersonic shear layer. *International Journal for Numerical Methods in Fluids* 1990; **10**:411–428.
30. Sirovich L. Turbulence and the dynamics of coherent structures, part 1: coherent structures. *Quarterly of Applied Mathematics* 1987; **45**(3):561–571.
31. Buhmann MD. Radial basis functions: theory and implementations. *Cambridge Monographs on Applied and Computational Mathematics*, 2003.
32. Kansa EJ. Multiquadrics—a scattered data approximation scheme with applications to computational fluid-dynamics—surface approximations and partial derivative estimates. *Computers and Mathematics with Applications* 1990; **19**(8/9):127–145.
33. Audze P, Englais V. New approach to planning out of experiments. *Problems of Dynamics and Strength* 1977; **35**(1):104–107.

DOI: 10.1002/fld